Mean-field description of ground-state properties of drip-line nuclei: Shell-correction method

W. Nazarewicz,[1,2,3,4] T.R. Werner,[1,2,3] and J. Dobaczewski[3]
[1]*Physics Division, Oak Ridge National Laboratory, P.O. Box 2008, Oak Ridge, Tennessee 37831*
[2]*Department of Physics and Astronomy, University of Tennessee, Knoxville, Tennessee 37996*
[3]*Institute of Theoretical Physics, Warsaw University, ul. Hoża 69, 00-681 Warsaw, Poland*
[4]*Joint Institute for Heavy-Ion Research, Oak Ridge, Tennessee 37831*
(Received 6 June 1994)

A shell-correction method is applied to nuclei far from the beta stability line, and its suitability to describe effects of the particle continuum is discussed. The sensitivity of predicted locations of one- and two-particle drip lines to details of the macroscopic-microscopic model is analyzed.

PACS number(s): 21.10.Dr, 21.10.Gv, 21.10.Pc, 21.60.−n

I. INTRODUCTION

The theoretical description of drip-line nuclei is one of the most exciting challenges today. The coupling between bound states and continuum invites strong interplay between various aspects of nuclear structure and reaction theory, and calculations have strong astrophysical implications, especially in the context of the r-process mechanism [1,2].

Theoretically, the physics of nuclei with very large values of neutron or proton excess is a challenge for well-established models of nuclear structure and, because of dramatic extrapolations involved, it invites a variety of theoretical approaches. Since the parameters of interactions used in the usual shell-model or mean-field calculations are determined so as to reproduce the properties of known nuclei, the parameters may not always be proper to be used in the calculation of drip-line nuclei. One hopes, however, that spectroscopy of exotic nuclei by means of a radioactive ion beam technique will lead to a better determination of forces, at least those interaction components that depend on isospin degrees of freedom.

The closeness of the Fermi level to the particle continuum makes the theoretical description of drip-line nuclei a very challenging task. To put things in some perspective, Fig. 1 displays the average potential wells, characteristic of a typical beta-stable system (^{120}Sn), a neutron drip-line system (^{150}Sn), and a proton drip-line system (^{100}Sn). While the low-energy structure of ^{120}Sn is almost exclusively determined by the particle-hole or pair excitations across the Fermi level from bound states to bound states (corrected for polarization effects due to giant vibrations), the lowest particle-hole or pair modes in drip-line nuclei are embedded in the particle continuum. Consequently, any tool of nuclear structure theory that aims at describing many-body correlations starting from the mean-field-based single-particle basis [such as shell-model, BCS, random phase approximation (RPA), etc.] has to be modified in the new regime.

One of the most important nuclear properties is its mass. The ability of a theoretical model to reproduce the nuclear binding energy is its ultimate test; it determines its reliability and practical usefulness. There exist many mass calculations (e.g., those based on the nuclear shell model) focused on a narrow region of the nuclear chart. These calculations are very successful in reproducing the data in a given region, but their applicability to other nuclei is limited. In order to extrapolate far from stability, large-scale global mass calculations are usually used (see, e.g., Refs. [3,4]). Since their parameters are optimized to reproduce known atomic masses, it is by no means obvious whether the particle number dependence predicted by global calculations at very large (or very small) values of the relative neutron excess,

$$I = \frac{N - Z}{A} , \tag{1.1}$$

is correct. In this context, a good example is the inclusion of the Coulomb redistribution energy term in the finite-range droplet model—strongly motivated by the recent mass measurements for the heaviest elements [5].

As far as the placement of nuclear drip lines is concerned, it is not the absolute value of nuclear mass but rather the *mass difference* between two isotopes that is of interest. The difference between binding energies, $B(Z,N)$, determines both the one-neutron sepa-

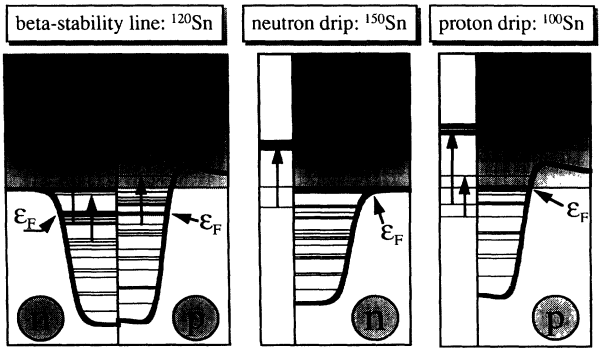

FIG. 1. Schematic illustration of coupling between bound states and particle continuum in drip-line nuclei. The potential wells are represented by the average Woods-Saxon field (plus Coulomb potential for protons).

ration energy, $S_n(Z,N) = B_n(Z,N) - B_n(Z,N-1)$, and the two-neutron separation energy, $S_{2n}(Z,N) = B_n(Z,N) - B_n(Z,N-2)$. If S_n becomes negative, then a nucleus is neutron unstable; the condition S_n=0 determines the position of the one-neutron drip line. By the same token, if S_{2n} becomes negative, a nucleus is unstable against the emission of two neutrons; the condition S_{2n}=0 determines the position of the two-neutron drip line. (Proton drip lines are defined analogously.)

Because of their sensitivity to various theoretical details, predicted drip lines are strongly model dependent [6–10]. The variations between predictions can be attributed to (i) fundamental differences between microscopic approaches, (ii) different effective interactions employed within the same approach, and (iii) different approximations used when solving the nuclear many-body problem within a given approach. In this study, several aspects of nuclear structure at the limits of extreme isospin are discussed by means of the macroscopic-microscopic approach. To test the influence of the particle continuum on shell corrections and pairing energies, we use the two versions of the shell-correction method with the Woods-Saxon average potential (first version is based on the standard averaging method and the second version is based on the semiclassical Wigner-Kirkwood expansion). In part II of this work [11], pairing properties of drip-line systems and the sensitivity of predictions to effective forces are investigated by means of self-consistent Hartree-Fock (HF) and Hartree-Fock-Bogolyubov (HFB) approaches.

II. SHELL-CORRECTION METHOD AND PARTICLE CONTINUUM

The main assumption of the shell-correction (macroscopic-microscopic) method [12–16] is that the total energy of a nucleus can be decomposed into two parts:

$$E = \tilde{E} + E_{\rm shell}, \tag{2.1}$$

where $\tilde{E}$ is the macroscopic energy (smoothly depending on the number of nucleons and thus associated with the "uniform" distribution of single-particle orbitals), and $E_{\rm shell}$ is the shell-correction term fluctuating with particle number reflecting the nonuniformities of the single-particle level distribution, i.e., shell effects. In order to make a separation (2.1), one starts from the one-body HF density matrix ρ,

$$\rho(x',x) = \sum_{i-{\rm occ}} \phi_i(x')\phi_i^*(x), \quad x = (\boldsymbol{r},\boldsymbol{\sigma}), \tag{2.2}$$

which can be decomposed into a "smoothed" density $\tilde{\rho}$ and a correction $\delta\rho$, which fluctuates with the shell filling,

$$\rho = \tilde{\rho} + \delta\rho. \tag{2.3}$$

The density matrix $\tilde{\rho}$ can be expressed by means of the smoothed distribution numbers $\tilde{n}_i$,

$$\tilde{\rho}(x',x) = \sum_i \tilde{n}_i\phi_i(x')\phi_i^*(x). \tag{2.4}$$

When considered as a function of the single-particle energies ϵ_i, the numbers $\tilde{n}_i$ vary smoothly in an energy interval of the order of the energy difference between major shells. The $\tilde{n}_i$'s can, in principle, take values smaller than zero and larger than unity [15]. Consequently, they do not represent the single-particle occupations in the strict sense.

In order to justify Eq. (2.1), the expectation value of a HF Hamiltonian (containing the kinetic energy, t, and the two-body interaction, $\bar{v}$) can be written in terms of $\tilde{\rho}$ and $\delta\rho$ [15,17]:

$$E_{\rm HF} = {\rm Tr}(t\rho) + \frac{1}{2}{\rm Tr}\,{\rm Tr}(\rho\bar{v}\rho) = \tilde{E} + E_{\rm osc} + O(\delta\rho^2), \tag{2.5}$$

where

$$\tilde{E} = {\rm Tr}(t\tilde{\rho}) + \frac{1}{2}{\rm Tr}\,{\rm Tr}(\tilde{\rho}\bar{v}\tilde{\rho}) \tag{2.6}$$

is the average part of $E_{\rm HF}$ and

$$E_{\rm osc} = {\rm Tr}(\tilde{h}_{\rm HF}\delta\rho) \quad \left[\tilde{h}_{\rm HF} = t + {\rm Tr}(\bar{v}\tilde{\rho})\right] \tag{2.7}$$

is the first-order term in $\delta\rho$ representing the shell-correction contribution to $E_{\rm HF}$. If a deformed average potential gives a similar spectrum to the averaged HF potential $\tilde{h}_{\rm HF}$, then the oscillatory part of $E_{\rm HF}$, given by Eq. (2.7), is very close to that of the deformed shell model, $E_{\rm shell}\approx E_{\rm osc}$. The second-order term in Eq. (2.5) is usually very small and can be neglected [18]. The above relation, known as the *Strutinsky energy theorem*, makes it possible to calculate the total energy using the non-self-consistent, deformed independent-particle model; the average part $\tilde{E}$ is usually replaced by the corresponding phenomenological liquid-drop (or droplet) model value, $E_{\rm macr}$. It is important that $E_{\rm shell}$ must not contain any regular (smooth) terms analogous to those already included in the phenomenological macroscopic part. (The extension of the energy theorem to the case with pairing is straightforward. The resulting expression for shell correction contains an additional contribution from the fluctuating part of the pairing energy; see Sec. V D.)

There are two single-particle level densities that define the shell correction. The (deformed) shell-model single-particle level density

$$g(\epsilon) = \sum_i \delta(\epsilon - \epsilon_i) \tag{2.8}$$

gives the single-particle energy, $E_{\rm s.p.}$. The smooth single-particle energy, $\tilde{E}_{\rm s.p.}$, is given by the mean single-particle level density, $\tilde{g}(\epsilon)$, obtained from $g(\epsilon)$ by folding with a smoothing function $f(x)$:

$$\tilde{g}(\epsilon) = \frac{1}{\gamma}\int_{-\infty}^{+\infty} d\epsilon' g(\epsilon') f\left(\frac{\epsilon-\epsilon'}{\gamma}\right) = \frac{1}{\gamma}\sum_i f\left(\frac{\epsilon-\epsilon_i}{\gamma}\right). \tag{2.9}$$

In Eq. (2.9), γ is the smoothing range; it should be larger than the typical distance between major shells. As follows from Eqs. (2.7)–(2.9), the shell correction can be

calculated by taking the difference between the sum of occupied levels and its average value, i.e.,

$$E_{\rm shell} = E_{\rm s.p.} - \tilde{E}_{\rm s.p.} = \sum_{i-{\rm occ}} \epsilon_i - \int_{-\infty}^{\tilde{\lambda}} \epsilon\, \tilde{g}(\epsilon) d\epsilon, \quad (2.10)$$

where $\tilde{\lambda}$ is the smoothed Fermi level defined through the particle-number equation

$$N = \int_{-\infty}^{\tilde{\lambda}} \tilde{g}(\epsilon) d\epsilon. \quad (2.11)$$

The folding function $f(x)$ can be written as a product,

$$f(x) = \omega(x) P_p(x), \quad (2.12)$$

where $\omega(x)$ is a weighting function and $P_p(x)$ is the so-called curvature-correction polynomial of the pth order. The smoothing procedure should be *unambiguous*; i.e., the averaging should extract only the fluctuating part, leaving the smooth part untouched. This condition defines $P_p(x)$ for any specific choice of $\omega(x)$. For instance, for the infinite potential well and a Gaussian weighting function, $\omega(x) = \pi^{-1/2}\exp(-x^2)$, the curvature-correction polynomial can be expanded in a finite series of Hermite polynomials of even order [15,19],

$$P_p(x) = \sum_{k=0,2,\ldots}^{p} \frac{(-1)^{k/2}}{2^k (k/2)!} H_k(x). \quad (2.13)$$

[For other examples of $f(x)$, see Ref. [20].]

The smoothed single-particle energy can be expressed in the form [20]

$$\tilde{E}_{\rm s.p.} = \int_{-\infty}^{\tilde{\lambda}} \epsilon\, \tilde{g}(\epsilon) d\epsilon = \sum_i \epsilon_i \tilde{n}_i + \gamma \frac{d\tilde{E}_{\rm s.p.}}{d\gamma}, \quad (2.14)$$

where the smoothed distribution numbers are

$$\tilde{n}_i = \frac{1}{\gamma} \int_{-\infty}^{\tilde{\lambda}} d\epsilon\, f\left(\frac{\epsilon - \epsilon_i}{\gamma}\right). \quad (2.15)$$

Since the value of $\tilde{E}_{\rm s.p.}$ should not depend on the smoothing range γ (or on the order of curvature correction p), the second term in Eq. (2.14) must vanish, i.e.,

$$\frac{d\tilde{E}_{\rm s.p.}}{d\gamma} = 0 \quad \left(\frac{d\tilde{E}_{\rm s.p.}}{dp} = 0\right). \quad (2.16)$$

If the above *plateau condition* does not hold, the Strutinsky averaging method does not yield an unambiguous result.

The treatment of the particle continuum in the shell-correction approach is an old problem. For finite-depth potentials, the sum in Eq. (2.9) should be replaced by a sum over bound single-particle states and an integral over positive-energy single-particle continuum, i.e.,

$$\sum_i \rightarrow \sum_{i-{\rm bound}} + \int_0^{\infty} d\epsilon\, \Delta g_{\rm cont}(\epsilon), \quad (2.17)$$

where $\Delta g_{\rm cont}$ is the continuum shell level density [21,22],

$$\Delta g_{\rm cont}(\epsilon) = \frac{1}{\pi} \frac{d\delta_\epsilon}{d\epsilon}, \quad (2.18)$$

and δ_ϵ is the corresponding phase shift (calculated for all partial waves).

Already in 1970 Lin [23] pointed out that the contribution from the particle continuum can affect the value of $E_{\rm shell}$, even for nuclei at the beta-stability line. In particular, he considered the positive-energy continuum in the energy interval $0 < \epsilon < 20$ MeV to calculate the neutron shell correction for ^{208}Pb. No plateau in $\tilde{E}_{\rm s.p.}$ was obtained and the result turned out be strongly γ and p dependent. Soon afterwards Ross and Bhaduri [24] carried out calculations along the same lines as in Ref. [23] and demonstrated that, by taking into account contributions from all neutron resonances up to ~100 MeV in ^{208}Pb, the plateau condition (2.16) could be met.

Bolsterli *et al.* [19] made an attempt to simulate the effect of the continuum by using the *quasibound states*, i.e., the states resulting from the diagonalization of a finite potential in a large harmonic-oscillator basis. The authors suggested a "working" prescription (the number of oscillator shells should not be too large, $N_{\rm osc}$~12), but no systematic analysis was carried out. (Later it was shown in Ref. [25] that the inclusion of quasibound states requires relatively high correction orders.) In the following, the Strutinsky averaging procedure including quasibound states will be referred to as the standard averaging method (SAM).

There have been some suggestions on how to generalize the Strutinsky averaging procedure for finite potentials. Bunatian *et al.* [15] exploited only the bound states of a finite-depth single-particle potential and derived modified expressions for the curvature correction. This method was then improved and exploited in series of papers by Strutinsky and Ivanyuk [26–28]. For instance, Ref. [28] demonstrates that the standard way of computing shell corrections, based on quasibound states, leads to serious errors in theoretical predictions for masses, fission barriers, and deformation energies. They also pointed out that the uncontrolled smooth component in shell corrections, resulting from the incorrect treatment of continuum, can cause some renormalization of the parameters of the macroscopic energy formula, determined from fitting the nuclear masses. Unfortunately, the results discussed in Ref. [28] suggest that the renormalization procedure, based solely on bound states, produces very unstable shell corrections in cases when the upper limit of the averaging interval (i.e., the number of the highest single-particle level considered) approaches the actual number of particles. Actually, such a situation happens at the particle drip lines.

The proper treatment of resonances is not an easy task, especially for deformed systems. Therefore, other methods of dealing with continuum are more useful in practical applications. In 1973 Jennings proved [29] the equivalence between the Strutinsky approach and the semiclassical averaging based on the partition function method (Wigner-Kirkwood expansion). In the semiclassical approximation, the Fermi energy $\lambda_{\rm SC}$ is determined by

$$N = \mathcal{L}^{-1}_{\lambda_{SC}}\left(\frac{Z(\beta)}{\beta}\right), \tag{2.19}$$

and the smoothed energy of the system is

$$\tilde{E}_{SC} = N\lambda_{SC} - \mathcal{L}^{-1}_{\lambda_{SC}}\left(\frac{Z(\beta)}{\beta^2}\right), \tag{2.20}$$

where $\mathcal{L}$ denotes the Laplace transform and Z is the semiclassical partition function [30],

$$Z(\beta) = \frac{2}{h^3}\int e^{-\beta H_c}(1 + \hbar w_1 + \hbar^2 w_2 + \cdots)d^3p d^3r, \tag{2.21}$$

where H_c is the classical one-body Hamiltonian of the system and the w's are defined in terms of the one-body potential. The partition function method was shown to be an excellent tool for computing the average single-particle energy [31–34]. In particular, Ref. [31] contains an explicit numerical check of the equivalence between the Wigner-Kirkwood (WK) expansion and the full Strutinsky averaging with the correct treatment of resonances. (For more discussion, see Ref. [32], Table I.)

III. WOODS-SAXON MODEL AND THE PARTICLE CONTINUUM

The deformed shell model used in this study is assumed to be of the form of the average deformed Woods-Saxon (WS) potential, which contains a central part, a spin-orbit term, and a Coulomb potential for protons. All these terms depend explicitly on a set of external (axial) deformation parameters, β_λ, defining the nuclear surface:

$$R(\theta;\boldsymbol{\beta}) = C(\boldsymbol{\beta})r_0 A^{1/3}\left[1 + \sum_\lambda \beta_\lambda Y_{\lambda 0}(\theta)\right], \tag{3.1}$$

where the coefficient C assures that the total volume enclosed by the surface [Eq. (3.1)] is conserved.

The deformed WS potential is assumed in the form [35]

$$V(\boldsymbol{r}) = V_0\left[1 + \kappa_0 I\right] f(\boldsymbol{r}), \tag{3.2a}$$

$$f(\boldsymbol{r}) = \frac{1}{1 + \exp\left[\xi(\boldsymbol{r})/a\right]}, \tag{3.2b}$$

where the function $\xi(\boldsymbol{r})$ is equal to the (perpendicular) distance (taken with the minus sign inside the surface) between the point $\boldsymbol{r}$ and the nuclear surface represented by Eq. (3.1). The diffuseness parameter a is independent of Z and N. This choice of the WS potential guarantees that the diffuse region of the potential is constant independently of the nuclear deformation.

The deformed spin-orbit (SO) potential is

$$V_{SO}(\boldsymbol{r}) = -\frac{\kappa}{M}\left(\nabla f_{SO} \times \boldsymbol{p}\right)\cdot\boldsymbol{s}. \tag{3.3}$$

Here κ is a (dimensionless) SO strength factor and

$$f_{SO}(\boldsymbol{r}) = \frac{1}{1 + \exp\left[\xi_{SO}(\boldsymbol{r})/a_{SO}\right]} \tag{3.4}$$

is a WS form factor. [Since the radius of the SO potential, r_{0-SO}, is, in general, different from the radius of the central part, the distance function entering Eq. (3.4) is indicated by ξ_{SO}.]

The Coulomb potential for protons, V_C, is assumed to be that of the charge $(Z-1)e$ distributed with the charge density $\rho_C(\boldsymbol{r}) = \rho_0 f(\boldsymbol{r})$, where $f(\boldsymbol{r})$ is the WS form factor of Eq. (3.2b). In our study we employed the set of WS parameters introduced in Ref. [36]. These parameters have been widely used in nuclear structure calculations around the beta-stability line and for neutron-rich nuclei. So far, no attempt has been made to optimize these parameters for very neutron-rich nuclei.

The eigenstates of the WS Hamiltonian

$$H_{WS} = T + V + V_{SO} + \tfrac{1}{2}(1 + \tau_3)V_C \tag{3.5}$$

are found by means of the expansion method in the axially deformed harmonic-oscillator basis. The oscillator frequencies, $\hbar\omega_\perp$ and $\hbar\omega_z$, have been optimized according to Ref. [35]. In our calculations we used *all* basis states belonging to $N \leq N_{osc}$ (stretched) oscillator shells.

The pattern of eigenstates of the WS Hamiltonian (3.5), as a function of the number of harmonic-oscillator quanta included in the basis ($10 \leq N_{osc} \leq 50$), is displayed in Fig. 2. The left portion shows the results representative of the spherical shape. [Note that every single-

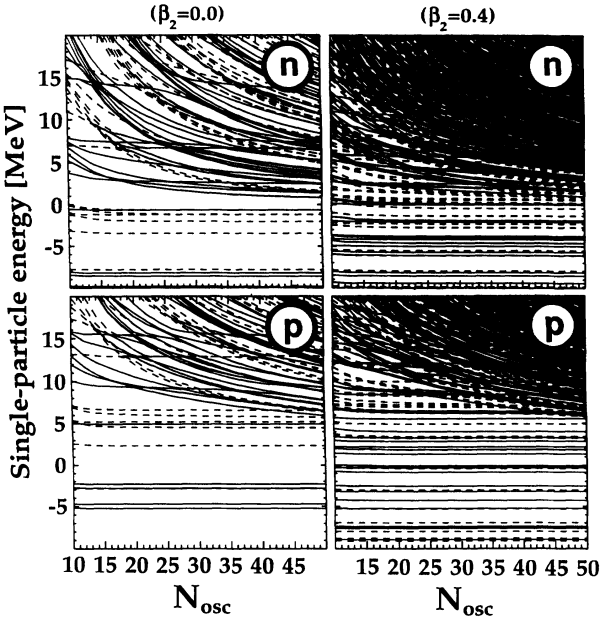

FIG. 2. Single-particle energies of the WS Hamiltonian (3.5) for neutrons (top) and protons (bottom) in ^{120}Sn as functions of N_{osc} (the number of harmonic-oscillator quanta included in the basis). The solid (dashed) lines correspond to $\pi = +$ ($\pi = -$) orbitals. The left portion displays the results for spherical shape (β_2=0); here every single-particle orbital is $(2j+1)$-fold degenerate. The results characteristic of deformed shapes (β_2=0.4) are shown in the right portion; each orbital is twofold degenerate due to time-reversal symmetry.

particle orbital is $(2j+1)$-fold degenerate.] The spherical symmetry is lifted in the right portion, representative of the deformed situation (β_2=0.4; here each orbital is only twofold degenerate due to the time reversal symmetry). It is seen that the energies of bound states ($\epsilon_i < 0$) converge very rapidly with the size of the basis; the convergence is achieved for $N_{\rm osc}\approx 14$. The positive-energy quasibound states representing the discretized particle continuum vary dramatically with $N_{\rm osc}$. Asymptotically, as the basis becomes infinite, quasibound states approach zero energy (cf. Fig. 18 of Ref. [19] and related discussion). This leads to an increased single-particle level density at $\epsilon_i > 0$ at large $N_{\rm osc}$ values. The only states which are not strongly affected in the considered interval of $N_{\rm osc}$ are the high-j orbitals which are fairly well localized inside a pocket in the centrifugal barrier created at positive energies by the mean-field potential.

The situation in protons is slightly less dramatic than in neutrons. Because of the presence of the Coulomb barrier (~9 MeV in ^{120}Sn), the positive-energy single-particle states below ~5 MeV are fairly stable. (They represent narrow subbarrier resonances, interesting in the context of proton emitters.) Judging from the results shown in Fig. 2, it is impossible to find an "optimal" value of $N_{\rm osc}$, at which the positive-energy quasibound spectrum would become a fair representation of physical continuum (resonances).

Since, at the particle drip lines, the radial asymptotics of wave functions are particularly important, it is instructive to relate $N_{\rm osc}$ to the radial dimensions of the harmonic-oscillator wave function. Its size depends both on the principal quantum number, N, and on the orbital quantum number, ℓ. The classical major axis of the orbit (N,ℓ) is given by [37]

$$(r_{\rm max})^2 \approx L^2\left[N+\sqrt{N^2-\ell^2}\right], \tag{3.6}$$

where $L=\sqrt{\frac{\hbar}{M\omega_0}}$ is the oscillator length; i.e., for the ℓ=0 oscillator states, the classical outer turning point is $r_{\rm max}\approx L\sqrt{2N}$. A weak dependence of $r_{\rm max}$ on N makes it very difficult, if not impossible, to describe the asymptotic radial behavior of the wave function using the expansion method in the harmonic-oscillator basis. From this point of view, the direct integration of the Schrödinger equation in a spatial box is superior. For instance, for the nucleus ^{120}Sn discussed in Fig. 2, the oscillator length L appearing in Eq. (3.6) equals to about 2 fm; hence $r_{\rm max}\simeq 10$ fm for N=12 and $r_{\rm max}\simeq 20$ fm for N=50. (For a pedagogical example, see Fig. 19 of Ref. [19].) By the same token, for a high-ℓ orbit with $\ell=N$ the major axes are $r_{\rm max}\simeq 7$ fm and 14 fm for N=12 and N=50, respectively.

IV. WIGNER-KIRKWOOD SEMICLASSICAL EXPANSION

The semiclassical approximation for a one-body Hamiltonian, including SO interaction, was developed in Ref. [31]. Denoting by $U(\boldsymbol{r})$ a one-body potential without the SO interaction,

$$U(\boldsymbol{r}) = V(\boldsymbol{r}) + \tfrac{1}{2}(1+\tau_3)\,V_C(\boldsymbol{r}), \tag{4.1}$$

the particle-number equation (2.19) takes the form

$$N = \frac{1}{3\pi^2}\left(\frac{2M}{\hbar^2}\right)^{\frac{3}{2}}\int^{r_{\rm SC}} d^3r\left\{(\lambda_{\rm SC}-U)^{\frac{3}{2}} + \frac{\hbar^2}{2M}\left[\tfrac{3}{4}\kappa^2(\boldsymbol{\nabla}f_{\rm SO})^2(\lambda_{\rm SC}-U)^{\frac{1}{2}} - \tfrac{1}{16}\nabla^2U(\lambda_{\rm SC}-U)^{-\frac{1}{2}}\right]\right\}. \tag{4.2}$$

The integral is cut off at the classical turning point (more precisely, the surface of turning points) defined by the relation $U(\boldsymbol{r}_{\rm SC}) = \lambda_{\rm SC}$. Equation (4.2) for $\lambda_{\rm SC}$ is solved iteratively. The expression (2.20) for the smoothed energy is slightly more complicated. In analogy to the notation introduced in Ref. [31], we may write

$$\tilde{E}_{\rm SC} = \lambda_{\rm SC}N - \left[E^0_{-3}+E^0_{-1}+E^0_{+1}\right] - \left[E^{\rm SO}_{-1}+E^{\rm SO}_{+1}\right], \tag{4.3}$$

where

$$E^0_{-3} = \frac{2}{15\pi^2}\left(\frac{2M}{\hbar^2}\right)^{\frac{3}{2}}\int^{r_{\rm SC}} d^3r(\lambda_{\rm SC}-U)^{\frac{5}{2}}, \tag{4.4}$$

$$E^0_{-1} = -\frac{1}{24\pi^2}\left(\frac{2M}{\hbar^2}\right)^{\frac{1}{2}}\int^{r_{\rm SC}} d^3r(\lambda_{\rm SC}-U)^{\frac{1}{2}}\nabla^2U, \tag{4.5}$$

$$\begin{aligned}E^0_{+1} = \frac{1}{5760\pi^2}\left(\frac{\hbar^2}{2M}\right)^{\frac{1}{2}}\int^{r_{\rm SC}} d^3r\frac{1}{(\lambda_{\rm SC}-U)^{\frac{1}{2}}(\boldsymbol{\nabla}U)^2}\{&-7\nabla^4U(\boldsymbol{\nabla}U)^2+5(\nabla^2U)^3\\ &+10[\boldsymbol{\nabla}U\cdot\boldsymbol{\nabla}(\nabla^2U)]\nabla^2U-5(\nabla^2U)^2\boldsymbol{\nabla}U\cdot\boldsymbol{\nabla}(\boldsymbol{\nabla}U)^2/(\boldsymbol{\nabla}U)^2\\ &+(\nabla^2U)\nabla^2(\boldsymbol{\nabla}U)^2+\boldsymbol{\nabla}U\cdot\boldsymbol{\nabla}\nabla^2(\boldsymbol{\nabla}U)^2-\nabla^2(\boldsymbol{\nabla}U)^2\boldsymbol{\nabla}U\cdot\boldsymbol{\nabla}(\boldsymbol{\nabla}U)^2/(\boldsymbol{\nabla}U)^2\},\end{aligned} \tag{4.6}$$

$$E^{\rm SO}_{-1} = \frac{\kappa^2}{6\pi^2}\left(\frac{2M}{\hbar^2}\right)^{\frac{1}{2}}\int^{r_{\rm SC}} d^3r(\lambda_{\rm SC}-U)^{\frac{3}{2}}(\boldsymbol{\nabla}f_{\rm SO})^2, \tag{4.7}$$

and

$$E_{+1}^{\mathrm{SO}}=\frac{\kappa^2}{48\pi^2}\left(\frac{\hbar^2}{2M}\right)^{\frac{1}{2}}\int^{r_{\mathrm{SC}}}d^3r(\lambda_{\mathrm{SC}}-U)^{\frac{1}{2}}\Big\{\tfrac{1}{2}\nabla^2(\nabla f_{\mathrm{SO}})^2-(\nabla^2 f_{\mathrm{SO}})^2$$
$$+\nabla f_{\mathrm{SO}}\cdot\nabla(\nabla^2 f_{\mathrm{SO}})-\frac{(\nabla f_{\mathrm{SO}})^2\nabla^2 U}{2(\lambda_{\mathrm{SC}}-U)}-2\kappa\Big[(\nabla f_{\mathrm{SO}})^2\nabla^2 f_{\mathrm{SO}}$$
$$-\tfrac{1}{2}\nabla f_{\mathrm{SO}}\cdot\nabla(\nabla f_{\mathrm{SO}})^2\Big]+2\kappa^2(\nabla f_{\mathrm{SO}})^4\Big\}. \tag{4.8}$$

Some technical details of the calculations of the above integrals, specific to our WS model, are discussed in Appendixes A and B.

The WK expansion [(4.2) and (4.3)] is only applicable for one-body potentials whose first and higher derivatives exist. This means that the method cannot be directly applied to a wide class of single-particle models based on the average field obtained by means of folding over a sharp generating potential or a sharp density distribution. Examples here are the folded Yukawa potential [19] or the Coulomb potential generated by the uniform density distribution; both are continuous in their values and first derivatives, but are discontinuous in their second and higher derivatives.

V. RESULTS

A. Quasibound states in the shell-correction method

The dependence of the shell correction (2.10) on the size of the oscillator basis and deformation is shown in Fig. 3 for a neutron-rich system (^{100}Zr) and a neutron drip-line nucleus (^{122}Zr). In the calculations all the quasibound states up to a cutoff energy of $131.2\,\mathrm{MeV}/A^{1/3}$ above the Fermi level were included. As expected, due to the effect of increased density of quasibound states with N_{osc}, the shell correction is unstable. It decreases or increases linearly with N_{osc}, depending on the position of the Fermi level. Indeed, for ^{100}Zr the value of E_{shell} slowly increases with N_{osc}, while the opposite effect is seen for ^{122}Zr. The reason for this different behavior is explained in Fig. 4 which shows the mean single-particle level density (2.9) as a function of single-particle energy ϵ for ^{100,122}Zr. For relatively low values of N_{osc} (e.g., N_{osc}=12–14), the average level density increases monotonically and it depends weakly on p (results for p=6 and p=12 are very similar). On the other hand, for N_{osc}=50, there appears an artificial local minimum in $\tilde{g}(\epsilon)$ located at $-7\lesssim\epsilon\lesssim-5\,\mathrm{MeV}$ which is caused by a rapid change in slope of $\tilde{g}(\epsilon)$ due to a large number of quasibound states at $\epsilon\gtrsim0$. This fluctuation is caused by a polynomial correction; as seen in Fig. 4 the results for N_{osc}=50 strongly depend on p. The smooth single-particle energy is obtained by integrating the product $\tilde{g}(\epsilon)\epsilon$ up to the Fermi level $\tilde{\lambda}$; cf. Eq. (2.14). Since $\tilde{g}(\tilde{\lambda})_{N_{\mathrm{osc}}=14}<\tilde{g}(\tilde{\lambda})_{N_{\mathrm{osc}}=50}$

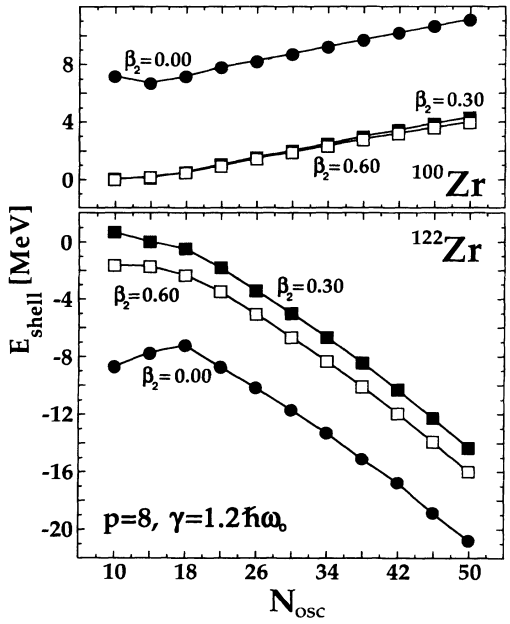

FIG. 3. Neutron shell correction for ^{100}Zn (top) and ^{122}Zr (bottom) for three quadrupole deformations, β_2=0, 0.3, 0.6, as a function of the number of harmonic-oscillator quanta included in the basis. For the SAM calculations we have used $\gamma=1.2\,\hbar\omega_0=49.2\,\mathrm{MeV}/A^{1/3}$ and an eighth-order curvature correction (p=8). All single-particle levels lying below a cutoff energy of $\epsilon_{\mathrm{cut}}=3.2\,\hbar\omega_0=131.2\,\mathrm{MeV}/A^{1/3}$ above the Fermi level were included.

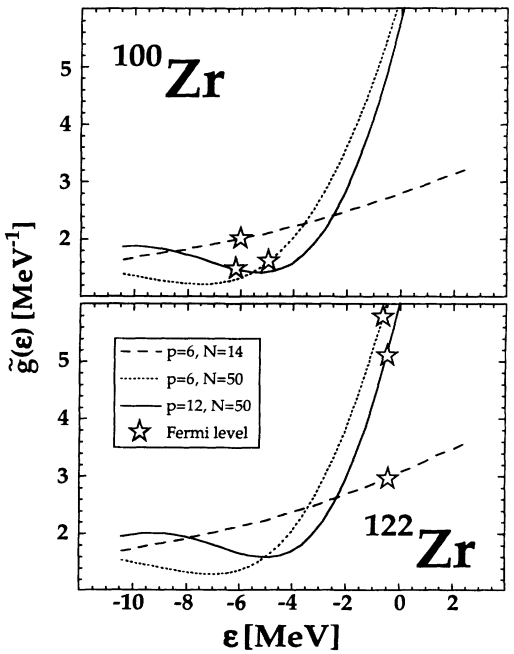

FIG. 4. Neutron average level density $\tilde{g}$ for ^{100}Zn (top) and ^{122}Zr (bottom) for β_2=0.3 as a function of single-particle energy ϵ. For the SAM calculations we have used the value of $\gamma=1.2\,\hbar\omega_0$ and $\epsilon_{\mathrm{cut}}=3.2\,\hbar\omega_0$. The average Fermi energies $\tilde{\lambda}$ are indicated by stars.

for ^{122}Zr (opposite holds for ^{100}Zr), this explains the tendency seen in Fig. 3.

The instability of the shell correction with respect to $N_{\rm osc}$ means that the total mass of a drip-line nucleus cannot be estimated by means of the SAM. Moreover, since in different isotopes one obtains a different dependence on $N_{\rm osc}$, the two-neutron separation energies are also affected. In fact, as seen in Fig. 3 the deformation energies can also be contaminated by the $N_{\rm osc}$ dependence. The relative values of $E_{\rm shell}$, computed at different deformations, vary with $N_{\rm osc}$ up to $N_{\rm osc}$=14 (^{100}Zr) and $N_{\rm osc}$=18 (^{100}Zr), while the recommended value of $N_{\rm osc}$ is 12–14 [19].

The results presented in this section demonstrate that the uncontrolled error in $E_{\rm shell}$ can seriously affect theoretical mass predictions for nuclei far from stability. If parameters of the macroscopic energy formula are determined by the global fit to experimental nuclear masses, some part of the unwanted effect of the continuum is absorbed by the isospin-dependent terms of the liquid-drop (or droplet) model mass formula.

B. Plateau condition in the shell-correction method

In Fig. 5, the total spherical shell corrections for ^{100}Zr and ^{122}Zr (i.e., including proton and neutron contributions) are plotted as a function of γ for different values of p. For the basis size we took the recommended value of $N_{\rm osc}$=12. Neither for ^{100}Zr nor for ^{122}Zr is the plateau condition (2.16) fulfilled exactly. However, while in the former case the fluctuations of $E_{\rm shell}$ with γ and p are rather weak (for the "usual" values of p=6, 8 and $\gamma/\hbar\omega_0$=1.0–1.2 the local plateau in $E_{\rm shell}$ is at ~6.7 MeV), in the latter case the variations in the shell correction are more dramatic and no unambiguous values can be extracted.

In the recent state-of-the-art large-scale mass calculations based on the folded Yukawa potential, Möller *et al.* [10] used $\gamma=\hbar\omega_0 B_s$ (B_s is the ratio of the actual nuclear surface to the spherical surface, i.e., B_s=1 at spherical shape), p=8, and $N_{\rm osc}$=12. They noted that, in contrast to light nuclei which have very low density of single-particle levels, the plateau condition is fulfilled for heavy nuclei. Our analysis suggests that for nuclei far from stability the plateau condition can also be violated.

C. Shell energies for the Wigner-Kirkwood smooth energy

In order to estimate the continuum-related uncertainty in the shell energy in typical SAM calculations, we performed a semiclassical analysis using the WK expansion. Figure 6 shows neutron shell corrections $E_{\rm shell}({\rm SAM})=E_{\rm s.p.}-\tilde{E}_{\rm s.p.}$ computed by means of the SAM, Eq. (2.14) ($N_{\rm osc}$=12, $\gamma=\hbar\omega_0$, p=8) as compared to $E_{\rm shell}({\rm WK})=E_{\rm s.p.}-\tilde{E}_{\rm SC}$ where the smoothed WK energy (4.3) is used. In both cases the same WS model was used. The calculations were carried out for the well-bound neutron systems ^{100}Zr and ^{166,186}Os ($\lambda_n<-6$ MeV), and for neutron drip-line nuclei ^{120,124}Zr and ^{206,226}Os ($-4<\lambda_n<-0.2$ MeV). The average deviation between $E_{\rm shell}$(SAM) and $E_{\rm shell}$(WK) ranges from ~0.4 MeV in ^{100}Zr and ^{166}Os to ~4.6 WeV in ^{124}Zr and ~7.6 MeV in

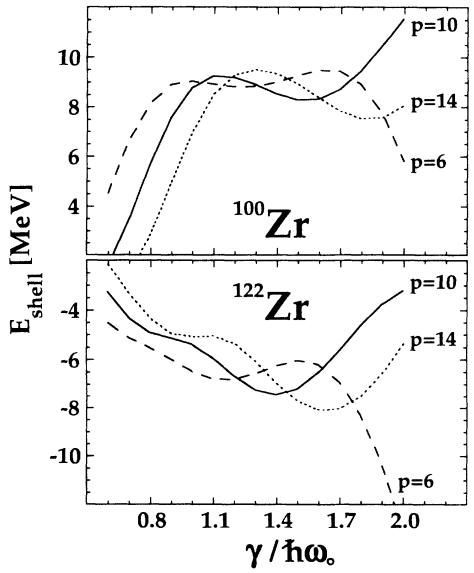

FIG. 5. Total shell correction at β_2=0 as a function of the smoothing range γ (in units of $\hbar\omega_0$) for ^{100}Zn (top) and ^{122}Zr (bottom). The three different curves correspond to p=6, 10, and 14. The number of basis states used in the diagonalization is $N_{\rm osc}$=12.

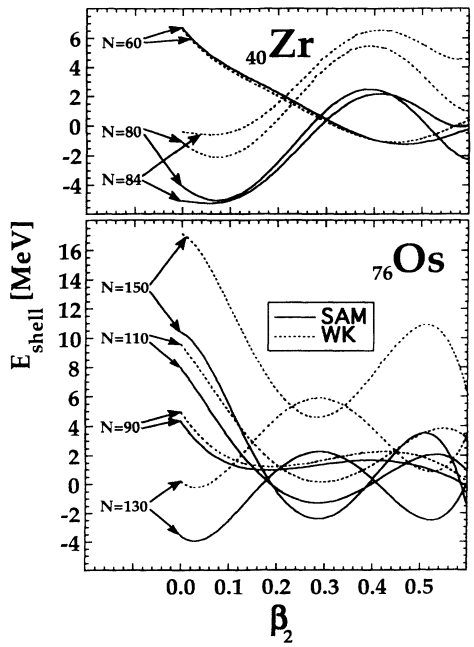

FIG. 6. Neutron shell corrections of the WS model, $E_{\rm shell}$(SAM) and $E_{\rm shell}$(WK), given by Eqs. (2.14) and (4.3), respectively, as a function of quadrupole deformation for ^{100,120,124}Zr (top) and ^{166,186,206,226}Os (bottom). The SAM smoothing was performed with $N_{\rm osc}$=12, $\gamma=\hbar\omega_0$, and p=8.

^{226}Os. Generally, for the neutron-rich systems, the shell corrections obtained by means of the SAM are lower than the semiclassical ones and the difference increases with N. Therefore, in the standard shell-correction calculations the nuclei around the neutron drip line are overbound. Another interesting result presented in Fig. 6 is that the difference between $E_{\rm shell}$(SAM) and $E_{\rm shell}$(WK) depends rather weakly on deformation. This suggests that one can approximate $E_{\rm shell}$ by

$$E_{\rm shell}(\beta) = E_{\rm shell}(\beta;\mathrm{SAM}) + E_{\rm shell}(\beta=0;\mathrm{WK}) - E_{\rm shell}(\beta=0;\mathrm{SAM}), \quad (5.1)$$

where the spherical semiclassical shell correction, $E_{\rm shell}(\beta=0;\mathrm{WK})$, involves calculating one-dimensional radial integrals only. The renormalization (5.1) can be particularly useful in the large-scale global mass calculations, such as those of Ref. [10]. However, one should keep in mind that this renormalization will not cure the problems related to the plateau condition and the dependence on $N_{\rm osc}$ discussed above.

It is worth noting that in the extended-Thomas-Fermi-with-Strutinsky-integral approach [8,38–40] the smooth energy entering their shell correction is defined by the semiclassical method [39]. Consequently, their shell corrections are free from the problems of the continuum.

D. Location of particle drip lines in the shell-correction method

In the macroscopic-microscopic method, the second contribution to the shell energy comes from pairing. Pairing correlations play a very special role in drip-line nuclei. This is seen from approximate HFB relations between the Fermi level, λ, pairing gap, Δ, and the particle separation energies. For instance, the neutron separation energies S_n and S_{2n} are given by [9,41]

$$S_n \approx -\lambda_n - \Delta, \quad (5.2)$$

$$S_{2n} \approx -2\lambda_n, \quad (5.3)$$

which leads to the following conditions for the one-neutron and two-neutron drip lines:

$$S_n = 0 \Longrightarrow \lambda_n + \Delta = 0, \quad (5.4)$$

$$S_{2n} = 0 \Longrightarrow \lambda_n = 0. \quad (5.5)$$

In particular, the condition (5.4) nicely illustrates the crucial role of the pairing interaction for determining the one-neutron drip line; it shows the equal importance of the single-particle field characterized by λ (determined by the particle-hole component of the effective interaction) and the pairing field, Δ (determined by the particle-particle part of the effective interaction). In fact, just around the particle drip lines, particle-hole and particle-particle channels are very strongly coupled, and the standard procedure based on a "two-step" treatment of the pairing Hamiltonian (i.e., computing pairing correlations *after* determining the single-particle basis) seems inappropriate.

In part II of our study [11], the pairing properties of drip-line nuclei are discussed using the self-consistent theory. Here, we only concentrate on the standard BCS or Lipkin-Nogami (LN) treatment of pairing correlations, which is used in the currently available large-scale mass calculations [8,10].

The macroscopic part of the total energy, $E_{\rm macr}$, already contains the average pairing energy, which accounts for the main part of the even-odd mass difference. Therefore, it is the fluctuating part of the pairing energy

$$E_{\rm shell}^{\rm (pair)} = E_{\rm pair} - \tilde{E}_{\rm pair} \quad (5.6)$$

that enters the expression for the total shell energy. The pairing correlation energy, $E_{\rm pair}$, is usually computed using a monopole pairing interaction with a constant (state-independent) strength G.

In this study, the BCS and LN equations were solved considering the N_p ($=Z$ or N) lowest single-particle orbitals. The average pairing strength, $G_{\rm avg}$, and the average pairing energy, $\tilde{E}_{\rm pair}$, were calculated according to the average gap method [16,19,42] in the version of Ref. [43]. We have also performed calculations using the fitted pairing strength $G_{\rm fit}$:

$$G_{\rm fit} A = G_0 + G_1 I, \quad (5.7)$$

where the constants G_0 and G_1 are obtained by a fit to odd-even mass differences in a given region of nuclei.

There is an obvious advantage of using $G_{\rm avg}$ rather than $G_{\rm fit}$ when going far from stability. Since $G_{\rm avg}$ is inversely proportional to the average single-particle level density at the Fermi level, $G_{\rm avg} \propto \tilde{g}(\tilde{\lambda})^{-1}$, this attenuates the influence of quasibound states on pairing properties. Figure 7 shows the neutron pairing gaps for the

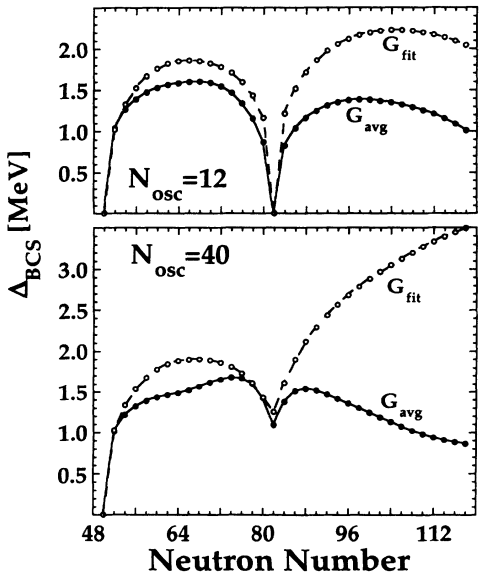

FIG. 7. Neutron BCS pairing gaps for the even tin isotopes as a function of N computed using the average pairing strength $G_{\rm avg}$ [43] (solid line) or the fitted pairing strength $G_{\rm fit}$ [Eq. (5.7) for G_0=19.2 MeV and G_1=−7.4 MeV, dashed line]. The single-particle spectrum (including quasibound states) was obtained by diagonalizing the WS Hamiltonian in $N_{\rm osc}$=12 (top) and $N_{\rm osc}$=40 (bottom) oscillator shells.

tin isotopes computed within the BCS approximation using $G_{\rm avg}$ or $G_{\rm fit}$. For neutron numbers $50 \leq N \lesssim 84$ both prescriptions for G yield fairly similar results. However, for higher neutron numbers the pairing gap obtained with $G_{\rm fit}$ is much larger that that computed with $G_{\rm avg}$, and the result strongly depends on the size of the single-particle basis. In particular, for $N_{\rm osc}=40$ the density of quasibound states is so large that $\Delta_n \neq 0$ for $N=82$. Since the pairing correction (5.6) behaves as Δ^2, the effect on $E_{\rm shell}^{\rm (pair)}$ is even more dramatic. Therefore, the contribution from quasibound states to the pairing correction is a source of another uncontrolled correction to the total energy in the macroscopic-microscopic method.

The total energy of the shell-correction method, Eq. (2.1), is divided into three parts:

$$E = E_{\rm macr} + E_{\rm shell}^{\rm (s.p.)} + E_{\rm shell}^{\rm (pair)}, \tag{5.8}$$

where $E_{\rm macr}$ is the macroscopic energy of the Yukawa-plus-exponential model of Refs. [44,45], $E_{\rm shell}^{\rm (s.p.)}$ is the shell correction (2.10), and $E_{\rm shell}^{\rm (pair)}$ is the pairing correction computed using the BCS procedure. (Results of the LN calculations are fairly similar and will not be discussed here.)

The predicted one- and two-neutron separation energies for the neutron-rich tin and lead isotopes are shown in Figs. 8 and 9, respectively. The two-neutron separation energies (top) were computed directly from binding energies of even-even nuclei. Since no self-consistent blocking was performed for odd nuclei, the one-neutron separation energies (bottom) were approximated by means of Eq. (5.2). As seen in Figs. 8 and 9, the influence of the continuum on the calculated positions of drip lines is quite significant. The two-neutron separation energies calculated in the WK method are systematically lower than those obtained in the SAM and the difference approaches ~1.6 MeV at $N=106$. This difference results in a shift in the position of the two-neutron drip line. According to the semiclassical approach, the nucleus $^{156}Sn_{106}$ appears at the two-neutron drip line, while in the SAM calculations there are several (~5) more stable even-even tin isotopes expected. A similar trend is seen in the position of the one-neutron drip line which in the SAM calculations is overestimated by 2–4 mass units.

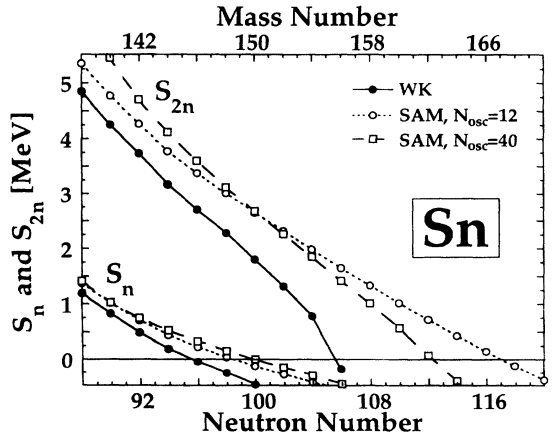

FIG. 8. One- and two-neutron separation energies for the even neutron-rich tin isotopes predicted in the shell-correction method with the WS average potential and the Yukawa-plus-exponential macroscopic model. The results based on the semiclassical Wigner-Kirkwood method (solid line) are compared with those obtained using the standard averaging including quasibound states. The smoothing was performed with $N_{\rm osc}=12$ (dotted line), or $N_{\rm osc}=40$ (dash-dotted line), $\gamma=\hbar\omega_0$, and $p=8$.

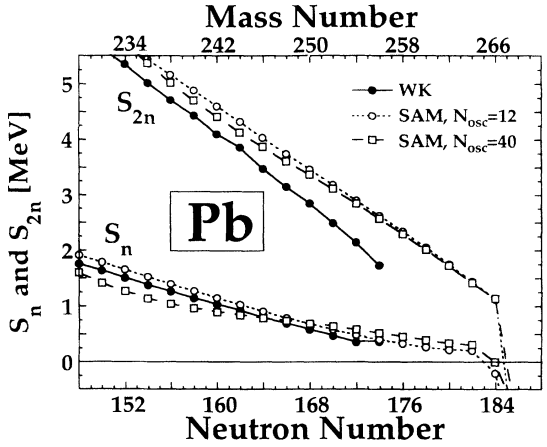

FIG. 9. Same as in Fig. 8 except for the neutron-rich lead isotopes.

E. Fermi-level self-consistency condition

For the lead isotopes the Fermi level in the WK method becomes positive at $N \sim 175$, and consequently no solution to the particle-number equation (4.2) can be found. At the same time, the value of S_{2n} for $N \sim 174$ is still positive (Fig. 9) and equals about 1.7 MeV. This constitutes a contradiction because, according to Eq. (5.3), the values of S_{2n} and λ_n should vanish simultaneously at the two-neutron drip line.

In the self-consistent theory (e.g., HF+BCS or HFB), the Fermi energy is equal to the derivative of the total energy (ground state energy of the even-even system) with respect to the particle number. However, in the shell-correction method this relation is violated due to the particle-number inconsistency inherent to the macroscopic-microscopic model. Differentiating both sides of Eq. (5.8) with respect to N (assuming the parameters of the one-body potential to be fixed), one obtains five different Fermi energies, namely,

$$\lambda_{\rm tot} = \lambda_{\rm macr} - \tilde{\lambda} + \lambda_{\rm s.p.} + \delta\lambda, \tag{5.9}$$

where $\lambda_{\rm tot}$ is related to the neutron separation energy, $\lambda_{\rm macr}$ represents the macroscopic Fermi energy, $\tilde{\lambda}$ (or $\lambda_{\rm SC}$ in the WK method) is the smoothed neutron Fermi energy, $\lambda_{\rm s.p.}$ is the neutron Fermi energy of the single-particle model obtained from the BCS equations, and $\delta\lambda$ contains contributions from the smoothed pairing en-

ergy and the proton shell correction. (The quantity $\delta\lambda$ is small and consequently is ignored in the following discussion to simplify the presentation.) It should be noted here that the finite-difference approximation to derivatives of the single-particle energy with respect to particle number (i.e., $\tilde{\lambda}$, $\lambda_{\rm SC}$, and $\lambda_{\rm s.p.}$) cannot be applied. (The deviation between derivatives and finite differences can be as large as 10 MeV.) The reason is that in the model based on the average one-body potential, the variation in the particle number (say, from N to $N+2$) leads to (i) the variation in the chemical potential and (ii) the variation in the average potential itself. Indeed, the parameters of the average potential depend smoothly on Z and N, and this causes a quite sizable change in single-particle level density with particle number.

In self-consistent approaches based on the two-body Hamiltonian, the requirement $\lambda_{\rm tot} = \lambda_{\rm s.p.}$ is fulfilled automatically. In the shell-correction method this requirement can be referred to as the *Fermi-level self-consistency condition*:

$$\lambda_{\rm macr}(Z,N) = \tilde{\lambda}(Z,N) \quad \text{or} \quad \lambda_{\rm macr}(Z,N) = \lambda_{\rm SC}(Z,N) \tag{5.10}$$

for the SAM or WK methods, respectively.

The parameters of the microscopic model are usually adjusted to selected single-particle properties of nuclei close to the beta-stability line, and the parameters of the macroscopic model are found by a global fit to masses and fission barriers. Therefore, it is not surprising that when extrapolating far from stability, the particle-number dependences of $\lambda_{\rm macr}$ and $\tilde{\lambda}$ are different. In Figs. 10 and 11 the Fermi energies defined in Eq. (5.9) are shown relative to $\lambda_{\rm macr}$ for the tin and lead isotopes, respectively. The degree of inconsistency in λ is measured by the magnitude of deviation $\Delta\lambda \equiv \tilde{\lambda} - \lambda_{\rm macr}$. It is seen that $|\Delta\lambda|$ is rather small around N=82 and N=126 for the tin and lead isotopes, respectively, and it reaches the value of about $\Delta\lambda$=1 MeV at drip lines.

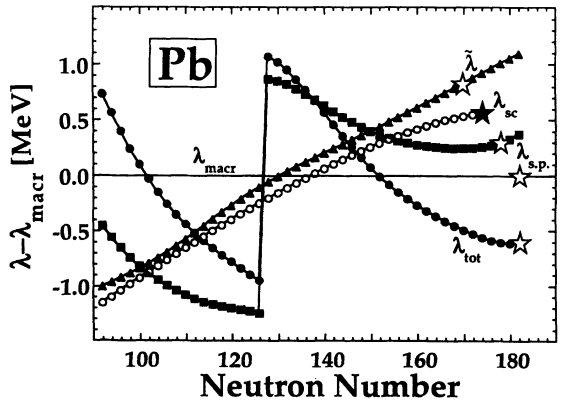

FIG. 10. Fermi energies of Eq. (5.9) relative to $\lambda_{\rm macr}$ as a function of N for the neutron-rich tin isotopes. The degree of the inconsistency in λ is measured by the magnitude of deviation $\tilde{\lambda} - \lambda_{\rm macr}$ (SAM variant) or $\lambda_{\rm SC} - \lambda_{\rm macr}$ (WK variant). The particle numbers at which $\lambda_{\rm tot}$=0, $\tilde{\lambda}$=0, $\lambda_{\rm SC}$=0, $\lambda_{\rm macr}$=0, and $\lambda_{\rm s.p.}$=0 are indicated by stars.

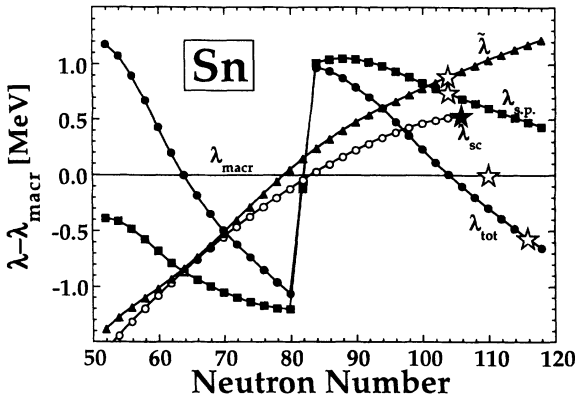

FIG. 11. Same as in Fig. 11 except for the neutron-rich lead isotopes.

The condition (5.10) defines a certain coupling between the macroscopic and microscopic parameters in the shell-correction method. Since $\Delta\lambda$ varies very smoothly as a function of N (see Figs. 10 and 11), the condition (5.10) is equivalent to

$$\lambda_{\rm macr}(Z,N_{\rm min}) = \lambda_{\rm SC}(Z,N_{\rm min}), \quad \lambda_{\rm macr}(Z,N_{\rm max}) = 0, \tag{5.11}$$

where, for a given atomic number Z, $N_{\rm min}$ and $N_{\rm max}$ are neutron numbers corresponding to proton- and neutron-drip-line isotopes, respectively. [$N_{\rm max}$ can be computed from Eq. (4.2) after putting $\lambda_{\rm SC} = 0$.]

The consistency between the microscopic and macroscopic parts of the energy in the shell-correction method has been discussed by several authors. In particular, Myers noticed [46], on the basis of the droplet model, that the parameters of the single-particle model (such as radius, potential depth, diffuseness) should be related to the parameters of the macroscopic model. In the global mass calculations by Möller *et al.* [10] the parameters defining the single-particle Hamiltonian do depend on the droplet model constants. In particular, as in Eq. (5.16), the depth of the folded-Yukawa potential depends linearly on the average bulk nuclear asymmetry of the droplet model, $\bar{\delta}$.

To illustrate condition (5.11), we performed calculations based on the WS average potential with parameters of Ref. [19], adjusted according to Myers [46]. Namely, we used

$$a = a_{\rm SO} = 0.9\frac{\ln 5}{\ln 9}\ [\rm fm] \tag{5.12}$$

for the diffuseness and

$$r_0 = r_{0-\rm SO} = R_0\left[1 - (a/R_0)^2\right]/A^{1/3}\ , \tag{5.13}$$

with

$$R_0 = R_\rho + 0.82 - 0.56/R_\rho\ , \tag{5.14}$$

for the radius. The radius R_ρ and the depth of the potential,

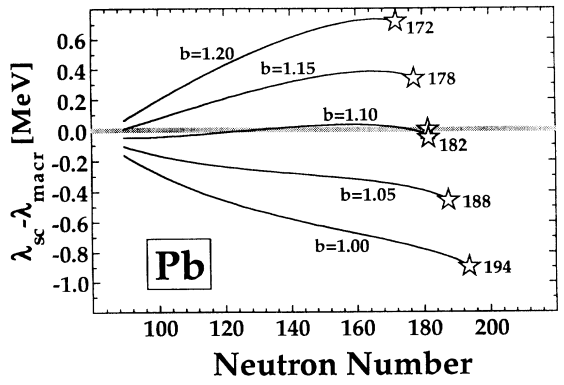

FIG. 12. Semiclassical Fermi energy, λ_{SC}, relative to λ_{macr} for the lead isotopes. The parameters of the WS model were taken according to Ref. [19]. The curves correspond to different values of the parameter b multiplying the neutron excess coefficient I entering through $\bar{\delta}$ the formula (5.16) for the neutron potential depth. The particle numbers $N=N_{max}$ at which $\lambda_{SC}=0$ and $\lambda_{macr}=0$ [Eq. (5.11)] are indicated by stars.

$$R_\rho = 1.16A^{1/3}(1+\bar{\epsilon})\ [\mathrm{fm}], \tag{5.15}$$

$$V_{n,p} = (52.5 \mp 48.7\bar{\delta})\ [\mathrm{MeV}]\ , \tag{5.16}$$

depend on the relative neutron excess coefficient I through

$$\bar{\delta} = \frac{I(1-0.0056A^{1/3}) + 0.0028A^{1/3}(1+I^2)}{1+3.15/A^{1/3}},$$

$$\bar{\epsilon} = -\frac{0.147}{A^{1/3}} + 0.33\bar{\delta}^2 + 0.00062A^{2/3}(1-I)^2. \tag{5.17}$$

Figure 12 shows $\Delta\lambda=\lambda_{SC}-\lambda_{macr}$ for the lead isotopes. Different curves were obtained by multiplying by a factor b (=1.00, 1.05, 1.10, 1.15, 1.20) the neutron excess coefficient I entering through $\bar{\delta}$ expression (5.16). (Direct renormalization of $\bar{\delta}$ is much less convenient since it leads to the modification of the isoscalar part of the potential depth.) As can be seen from Fig. 12, the standard value, b=1, gives values of λ_{SC} too small, in particular when the neutron number approaches N_{max}; the resulting value, N_{max}=194, is much larger than that of the macroscopic model, N=182 (as indicated in Fig. 12). However, by increasing the value of b by 10% conditions (5.11) can be met for the considered lead isotopes. It remains to be investigated whether the Fermi-level self-consistency condition can be consistently fulfilled for other isotopes.

VI. CONCLUSIONS

The main objective of this study was to investigate the influence of the particle continuum on the shell-correction energies of the macroscopic-microscopic method. The shell corrections obtained by means of the standard averaging method were compared with those calculated with the semiclassical Wigner-Kirkwood expansion technique. The systematic error in E_{shell}, due to the particle continuum, can be as large as several MeV at the neutron drip line. According to our calculations, this error depends weakly on deformation. This suggests a possibility of renormalizing E_{shell} only at the spherical shape.

As demonstrated in our study, the use of quasibound states as physical resonances can lead to serious deviations when extrapolating off beta stability. In particular, the associated theoretical error in predicted particle drip lines can be as large as ΔN=10. We also emphasized the role of the self-consistency condition between the microscopic and macroscopic Fermi energies. If this condition is violated, the relation between the Fermi energy and the separation energy is lost.

We hope that our work will be helpful for future global calculations of nuclear masses in the framework of the one-body (macroscopic-microscopic) description. As will be discussed in the forthcoming study based on self-consistent two-body procedures [11], there are also other uncertainties related, e.g., to the choice of the effective interaction. A deep understanding of the coupling between single-particle and pairing channels, and between discrete states and particle continuum, is a key to the physics of drip-line systems and a serious challenge for future work.

ACKNOWLEDGMENTS

Oak Ridge National Laboratory is managed for the U.S. Department of Energy by Martin Marietta Energy Systems, Inc. under contract No. DE-AC05-84OR21400. The Joint Institute for Heavy Ion Research has as member institutions the University of Tennessee, Vanderbilt University, and the Oak Ridge National Laboratory; it is supported by the members and by the Department of Energy through Contract No. DE-FG05-87ER40361 with the University of Tennessee. Theoretical nuclear physics research at the University of Tennessee is supported by the U.S. Department of Energy through Contract No. DE-FG05-93ER40770. This research was also supported by the Polish Committee for Scientific Research under Contract No. 20450 91 01.

APPENDIX A: SEMICLASSICAL APPROXIMATION TO THE WOODS-SAXON MODEL

The semiclassical equations (4.2) and (4.3) are defined through the high-order derivatives of average potentials entering the WS Hamiltonian. In order to calculate ∇V and $\nabla^2 V$, we took advantage of certain geometric relations specific to the definition of the WS potential (3.2). Figure 13 shows the surface geometry typical for an axial system; here the nuclear surface, $r=R(\theta)$, is given by Eq. (3.1). Given the radius point $\boldsymbol{r}=\boldsymbol{r}_{OB}$ (see Fig. 13) the function $\xi(\boldsymbol{r})$ represents the distance $\pm|\boldsymbol{r}_{AB}|$ [taken with the minus (plus) sign inside (outside) the surface $R(\theta)$]. Denoting by $\boldsymbol{n}$ [$\boldsymbol{n}=\nabla\xi(\boldsymbol{r})$] and $\boldsymbol{t}$ the normal and tangent unit vectors to the surface at point A, respectively, one can write

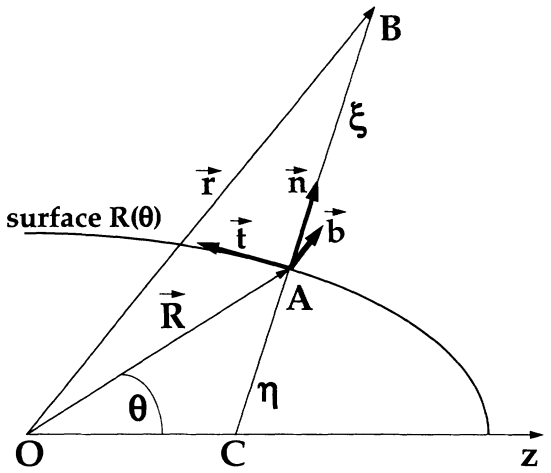

FIG. 13. Geometric relations between a vector point $\boldsymbol{r}$, the distance function $\xi(\boldsymbol{r})$, and the nuclear surface, $R(\theta)$. The unit vectors $\boldsymbol{n}$, $\boldsymbol{t}$, and $\boldsymbol{b}$ (normal, tangent, and binormal vector fields of R) represent the Frenet frame field on R.

$$\boldsymbol{r} = \boldsymbol{R} + \boldsymbol{n}\xi(\boldsymbol{r}), \tag{A1}$$

where $\boldsymbol{R}=\boldsymbol{r}_{OA}$. By acting with the gradient operator on both sides of Eq. (A1), one obtains

$$(\boldsymbol{\nabla n})\xi(\boldsymbol{r}) = 2 - \boldsymbol{\nabla R}. \tag{A2}$$

In order to calculate $\boldsymbol{\nabla R}$, one computes the gradient in the Frenet frame defined by three unit vectors $\boldsymbol{n}$, $\boldsymbol{t}$, and $\boldsymbol{b}=\boldsymbol{t}\times\boldsymbol{n}$. The result is

$$\boldsymbol{\nabla R} = \frac{\varrho}{\varrho+\xi} + \frac{\eta}{\eta+\xi}, \tag{A3}$$

where the curvature radius, ϱ, and $\eta=|\boldsymbol{r}_{AC}|$ are given by

$$\varrho = \frac{\left[R^2+R'^2\right]^{\frac{3}{2}}}{R^2+2R'^2-RR''}, \quad \eta = \frac{\left[R^2+R'^2\right]^{\frac{1}{2}}}{1-R'\cot\theta/R}, \tag{A4}$$

and $R'=dR/d\theta$ and $R''=d^2R/d\theta^2$. Finally, by means of Eqs. (A2)–(A4), one obtains

$$\boldsymbol{\nabla n} = \nabla^2\xi = \frac{1}{\varrho+\xi} + \frac{1}{\eta+\xi}. \tag{A5}$$

In the spherical case, $\xi(r) = r - R$, $\varrho = \eta = R$, and $\boldsymbol{\nabla n} = 2/r$, as expected. For given $\boldsymbol{r}$, the distance $\xi(\boldsymbol{r})$ and the vector R are calculated numerically by solving the equation $d|r - R(\theta)|/d\theta=0$. By denoting

$$V^{(n)}(\boldsymbol{r}) \equiv \frac{d^nV}{d\xi^n}, \tag{A6}$$

one can compute the derivatives appearing in Eqs. (4.2) and (4.3). For example,

$$\begin{aligned}\boldsymbol{\nabla}V^{(n)} &= V^{(n+1)}\boldsymbol{n},\\ (\boldsymbol{\nabla}V^{(n)})^2 &= (V^{(n+1)})^2,\\ \nabla^2V^{(n)} &= V^{(n+2)} + V^{(n+1)}\nabla^2\xi.\end{aligned} \tag{A7}$$

The derivatives higher than 2 involve quantities such as $\boldsymbol{n}\cdot\boldsymbol{\nabla}(\nabla^2\xi)$ or $\nabla^4\xi$ which are computed numerically by means of the finite-difference method. It is known that the standard parametrizations of the nuclear shape give rise to a singularity of higher derivatives at $r=0$, or to their large variations at $\theta=0°$ or $\theta=90°$ [47,48]. In order to achieve better accuracy of higher-order terms of the WK expansion, it has been assumed that the WS potential is constant for the values of $\xi(\boldsymbol{r})<\xi_{\rm crit} = -7a$. We have checked that up to $\beta_2\sim0.7$ the results are stable with respect to variations of $\xi_{\rm crit}$.

It is interesting to note that although $(\boldsymbol{\nabla}V)^2=(V^{(1)})^2$ is a simple analytic function of $\xi(\boldsymbol{r})$, the Laplacian ∇^2V depends both on $\xi(\boldsymbol{r})$ and θ; see Eqs. (A7) and (A5). This will lead to slight modifications of some discussion in Refs. [49,50], where ∇^2V was assumed to depend solely on the distance $\xi(\boldsymbol{r})$.

Special care should be taken when integrating singularities at $\lambda_{\rm SC} = U$ in Eqs. (4.2) and (4.3). A practical way of handling singularities at $\boldsymbol{r}_{\rm SC}$ is to employ the identity

$$\begin{aligned}\int_{r_{\rm min}}^{r_{\rm SC}} d^3r\frac{\Phi(\boldsymbol{r})}{\sqrt{\lambda_{\rm SC}-U}} &= \int_{r_{\rm min}}^{r_{\rm SC}} d^3r\frac{\Phi(r,\Omega)-\Phi(r_{\rm SC}(\Omega),\Omega)}{\sqrt{\lambda_{\rm SC}-U}} + 2\int d\Omega\, r_{\rm min}^2(\Omega)\frac{\Phi(r_{\rm SC}(\Omega),\Omega)}{(\partial U/\partial r)_{|r_{\rm min}(\Omega)}}\sqrt{\lambda_{\rm SC}-U(r_{\rm min}(\Omega),\Omega)}\\ &+2\int d\Omega\,\Phi(r_{\rm SC}(\Omega),\Omega)\int_{r_{\rm min}(\Omega)}^{r_{\rm SC}(\Omega)} dr\,\frac{r\sqrt{\lambda_{\rm SC}-U(r,\Omega)}}{(\partial U/\partial r)}\left[2-\frac{r\left(\partial^2U/\partial r^2\right)}{(\partial U/\partial r)}\right],\end{aligned} \tag{A8}$$

where $\Phi(\boldsymbol{r})$ is a function of $\boldsymbol{r}=(r,\Omega)$ and the integration is performed over the volume surrounded by the surfaces $r = r_{\rm min}(\Omega)$ and $r = r_{\rm SC}(\Omega)$. In the above equation, the singularity at $\boldsymbol{r}_{\rm SC}$ has been removed at the expense of generating singularity inside the classical region at $(\boldsymbol{\nabla}U)^2=0$. (Such a situation happens for the protons, due to different radial behaviors of WS and Coulomb potentials.) In practice, however, the identity (A8) is only used in the narrow region around $\boldsymbol{r}_{\rm SC}$ where $(\boldsymbol{\nabla}U)^2$ is never zero.

APPENDIX B: COULOMB POTENTIAL OF THE FERMI DISTRIBUTION

The Coulomb potential generated by the WS (Fermi) charge distribution (3.2b) is given by

$$V_C(\boldsymbol{r}) = \int d^3r'\frac{\rho_0}{1+\exp\left[\xi(\boldsymbol{r}')/a\right]}\frac{1}{|\boldsymbol{r}-\boldsymbol{r}'|}. \tag{B1}$$

In the axial case this integral can be reduced to two di-

mensions (with integrand involving complete elliptic integrals). Since

$$\nabla^2 V_C(\boldsymbol{r}) = -4\pi\rho_C(\boldsymbol{r}), \tag{B2}$$

the contributions from the Coulomb potential to higher-order derivatives in Eqs. (4.2) and (4.3) are calculated easily using expressions derived in Appendix A.

For a spherical shape, the angular integrations in Eq. (B1) can be performed explicitly to give

$$V_C(r) = \frac{4\pi}{r}\int_0^r dr'\, r'^2 \rho_C(r') + 4\pi\int_r^\infty dr'\, r'\rho_C(r'). \tag{B3}$$

Finally, the radial integrals are computed by means of identity

$$\frac{1}{1+\exp[(r-R)/a]} = \begin{cases} 1+\sum_{n=1}^{\infty}(-1)^n \exp[-n(R-r)/a] & \text{if } r < R, \\ -\sum_{n=1}^{\infty}(-1)^n \exp[-n(r-R)/a] & \text{if } r > R. \end{cases} \tag{B4}$$

The resulting fast-converging series gives V_C with desired accuracy.

[1] K.-L. Kratz, J.-P. Bitouzet, F.-K. Thielemann, P. Möller, and B. Pfeiffer, Astrophys. J. **403**, 216 (1993).
[2] W.M. Howard, S. Goriely, M. Rayet, and M. Arnould, Astrophys. J. **417**, 713 (1993).
[3] S. Maripuu, At. Data Nucl. Data Tables **17**, i (1976).
[4] P.E. Haustein, At. Data Nucl. Data Tables **39**, 185 (1988).
[5] P. Möller, J.R. Nix, W.D. Myers, and W.J. Swiatecki, Nucl. Phys. **A536**, 61 (1992).
[6] P. Möller, W.D. Myers, W.J. Swiatecki, and J. Treiner, At. Data Nucl. Data Tables **39**, 225 (1988).
[7] D. Hirata, H. Toki, T. Watabe, I. Tanihata, and B.V. Carlson, Phys. Rev. C **44**, 1467 (1991).
[8] Y. Aboussir, J.M. Pearson, A.K. Dutta, and F. Tondeur, Nucl. Phys. **A549**, 155 (1992); J.M. Pearson (private communication).
[9] R. Smolańczuk and J. Dobaczewski, Phys. Rev. C **48**, R2166 (1993).
[10] P. Möller, J.R. Nix, W.D. Myers, and W.J. Swiatecki, At. Data Nucl. Data Tables (to be published).
[11] J. Dobaczewski, W. Nazarewicz, and T.R. Werner (unpublished).
[12] W.J. Swiatecki, in *Proceedings of the 2nd International Conference on Nuclidic Masses, Vienna, 1963*, edited by W.H. Johnson, Jr. (Springer-Verlag, Vienna, 1964), p. 58.
[13] V.M. Strutinsky, Nucl. Phys. **A95**, 420 (1967).
[14] V.M. Strutinsky, Nucl. Phys. **A122**, 1 (1968).
[15] G.G. Bunatian, V.M. Kolomietz, and V.V. Strutinsky, Nucl. Phys. **A188**, 225 (1972).
[16] M. Brack, J. Damgård, A.S. Jensen, H.C. Pauli, V.M. Strutinsky, and C.Y. Wong, Rev. Mod. Phys. **44**, 320 (1972).
[17] P. Ring and P. Schuck, *The Nuclear Many-Body Problem* (Springer-Verlag, Berlin, 1980).
[18] M. Brack and P. Quentin, Nucl. Phys. **A361**, 35 (1981).
[19] M. Bolsterli, E.O. Fiset, J.R. Nix, and J.L. Norton, Phys. Rev. C **5**, 1050 (1972).
[20] M. Brack and H.C. Pauli, Nucl. Phys. **A207**, 401 (1973).
[21] E. Beth and G.E. Uhlenbeck, Physica **4**, 915 (1937).
[22] A.G. Petschek, Phys. Lett. **34A**, 411 (1971).
[23] W.-f. Lin, Phys. Rev. C **2**, 871 (1970).
[24] C.K. Ross and R.K. Bhaduri, Nucl. Phys. **A188**, 566 (1972).
[25] A. Sobiczewski, A. Gyurkovich, and M. Brack, Nucl. Phys. **A289**, 346 (1977).
[26] V.M. Strutinsky and F.A. Ivanjuk, Nucl. Phys. **A255**, 405 (1975).
[27] F.A. Ivanyuk and V.M. Strutinsky, Z. Phys. **A286**, 291 (1978).
[28] F.A. Ivanyuk and V.M. Strutinsky, Z. Phys. A **290**, 107 (1979).
[29] B.K. Jennings, Nucl. Phys. **A207**, 401 (1973).
[30] G.E. Uhlenbeck and E. Beth, Physica **3**, 729 (1936).
[31] B.K. Jennings, R.K. Bhaduri, and M. Brack, Phys. Rev. Lett. **34**, 228 (1975).
[32] B.K. Jennings and R.K. Bhaduri, Nucl. Phys. **A237**, 149 (1975).
[33] B.K. Jennings, R.K. Bhaduri, and M. Brack, Nucl. Phys. **A253**, 29 (1975).
[34] M. Brack and B.K. Jennings, Nucl. Phys. **A258**, 264 (1976).
[35] S. Ćwiok, J. Dudek, W. Nazarewicz, J. Skalski, and T.R. Werner, Comput. Phys. Commun. **46**, 379 (1987).
[36] J. Dudek, Z. Szymański, and T.R. Werner, Phys. Rev. C **23**, 920 (1981).
[37] A. Bohr and B.R. Mottelson, *Nuclear Structure* (W.A. Benjamin, New York, 1969), Vol. 1.
[38] Y.H. Chu, B.K. Jennings, and M. Brack, Phys. Lett. **68B**, 407 (1977).
[39] A.K. Dutta, J.-P. Arcoragi, J.M. Pearson, R. Behrman, and F. Tondeur, Nucl. Phys. **A458**, 77 (1986).
[40] J.M. Pearson, Y. Aboussir, A.K. Dutta, R.C. Nayak, M. Farine, and F. Tondeur, Nucl. Phys. **A528**, 1 (1991).
[41] M. Beiner, R.J. Lombard, and D. Mas, Nucl. Phys. **A249**, 1 (1975).
[42] S.T. Belyaev, Mat. Fys. Medd. Dan. Vid. Selsk. **31**, 11 (1959).
[43] P. Möller and J.R. Nix, Nucl. Phys. **A536**, 20 (1992).
[44] P. Möller and J.R. Nix, Nucl. Phys. **A361**, 117 (1981).
[45] P. Möller and J.R. Nix, At. Data Nucl. Data Tables **26**, 165 (1981).

[46] W.D. Myers, Nucl. Phys. **A145**, 387 (1970).
[47] J. Damgaard, H.C. Pauli, V.V. Pashkevich, and V.M. Strutinsky, Nucl. Phys. **A135**, 432 (1969).
[48] U. Götz, H.C. Pauli, and K. Adler, Nucl. Phys. **A175**, 481 (1971).
[49] J. Dudek, W. Nazarewicz, and P. Olanders, Nucl. Phys. **A420**, 285 (1984).
[50] R. Bengtsson, J. Dudek, W. Nazarewicz, and P. Olanders, Phys. Scr. **39**, 196 (1989).

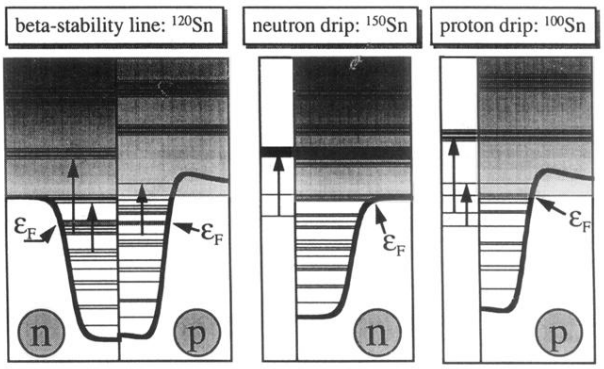

FIG. 1. Schematic illustration of coupling between bound states and particle continuum in drip-line nuclei. The potential wells are represented by the average Woods-Saxon field (plus Coulomb potential for protons).